Dispersion properties of vortex-type monatomic lattices

G. Carta[a,b,*], M. Brun[a,c], A.B. Movchan[c], N.V. Movchan[c], I.S. Jones[b]

[a]*Dipartimento di Ingegneria Meccanica, Chimica e dei Materiali, Universita' di Cagliari, Italy*
[b]*School of Engineering, John Moores University, Liverpool, UK*
[c]*Department of Mathematical Sciences, University of Liverpool, UK*

Abstract

The paper presents a systematic study of dispersive waves in an elastic chiral lattice. Chirality is introduced through gyroscopes embedded into the junctions of a doubly periodic lattice. Bloch-Floquet waves are assumed to satisfy the quasi-periodicity conditions on the elementary cell. New features of the system include degeneracy due to the rotational action of the built-in gyroscopes and polarisation leading to the dominance of shear waves within a certain range of values of the constant characterising the rotational action of the gyroscopes. Special attention is given to the analysis of Bloch-Floquet waves in the neighbourhoods of critical points of the dispersion surfaces, where standing waves of different types occur. The theoretical model is accompanied by numerical simulations demonstrating directional localisation and dynamic anisotropy of the system.

Keywords: wave propagation, elastic lattice, chirality, gyroscope, dispersion, wave polarisation, dynamic anisotropy

1. Introduction

Propagation of waves in periodic discrete media has received increasing attention in recent years, although the first studies date back several decades (Brillouin, 1953; Kittel, 1956). Particular emphasis has been devoted to elastic lattices (Marder and Liu, 1993; Slepyan, 2002; Brun et al., 2010; Colquitt et al., 2011, 2012), arrays of point masses connected by elastic rods or beams. Waves propagating in lattices are dispersive, even if the lattice is monatomic with uniform stiffness. Special properties, such as wave beaming and occurrence of band

---

gaps, are achieved by varying periodically the stiffness and the density of the lattice components.

Some lattices, with appropriately designed configurations, are characterised by an asymmetric property known as "chirality". This term was first used by Lord Kelvin (1894), according to whom an object is chiral "if its image in a plane mirror, ideally realized, cannot be brought to coincide with itself."

Chirality is exploited in electromagnetism to produce negative refraction (Pendry, 2004; Chern, 2013). In elasticity, Spadoni et al. (2009) analysed wave propagation in hexagonal chiral lattices proposed by Prall and Lakes (1997), investigating in particular the features of band gaps and the anisotropy of the medium at high frequencies, manifested in wave directionality. Brun et al. (2012) proposed a novel active chiral model, in which a system of gyroscopes (or gyros) was incorporated into both monatomic and biatomic lattices. The chirality derives from the micro-rotations of the lattice masses, transmitted by the motion of the gyroscopes. Numerical illustrations reveal that this chiral structure can be used as a cloak guiding waves around a defect.

Vector problems of in-plane elasticity are more challenging than scalar problems, typical of electromagnetic systems and of elastic media subjected to anti-plane shear loading. The difficulty arises from the co-existence of two types of waves within in-plane elasticity. Martinsson and Movchan (2003) analysed free vibrations of vector lattices and provided a general tool to tune the lattice properties such that band gaps appear in prescribed intervals of frequency.

The study by Brun et al. (2012) introduced monatomic and biatomic lattice systems with embedded gyros. This was a novel idea leading to unusual degeneracies and a coupling mechanism between shear and pressure waves. A homogenised chiral medium showed exciting filtering properties for frequency response problems. It remained a challenge to model forced lattice systems with built-in gyros in the high frequency regime. This challenge is addressed in the present paper to the extent that the critical points have been fully classified and the important effects of dynamic anisotropy have been studied.

The geometry of the model and the vectorial equations of motion are presented in Section 2. By employing Bloch-Floquet conditions, the dispersion relation of the medium is also derived, and its dispersive properties are examined in great detail in Section 3. More specifically, Section 3 contains a thorough description of the dispersion surfaces of the chiral lattice and their asymptotic approximations for the degenerate case when the value of the spinner constant, describing the effect of the gyros, is close to the value of the lattice masses. In addition, the wave polarisation, induced by the gyros, is quantified, thus addressing the challenges raised by the qualitative work by Brun et al. (2002). Furthermore, the strong dynamic anisotropy of the medium at high frequencies is investigated by analysing standing waves at saddle points. Finally, Section 4 presents simulations of frequency response problems for a chiral discrete system, which validate the conclusions drawn in Section 3. These computations focus, in particular, on illustrations of properties of the dynamic response of the system for frequencies chosen in the neighbourhoods of critical points of the dispersion surfaces. For these frequencies, classical homogenisation approximations are not

applicable, as shown by Movchan and Slepyan (2013). We note that the same frequency may correspond to several critical points on the dispersion surfaces. Special attention is given to directional preference and localisation induced by the rotational action of the gyros embedded into the lattice.

2. Structure and governing equations of the chiral medium

We consider a two-dimensional triangular lattice, consisting of equal particles of mass m connected by elastic links of length l, stiffness c and negligible mass. The chirality property is conferred on the medium by a system of gyros attached to the lattice particles, as shown in Fig. 1a. The axis of each gyro, which is perpendicular to the lattice plane in the initial configuration, changes its orientation when the particle to which it is connected moves in the x_1-x_2 plane. As a consequence, the gyro exerts on the particle a force that is orthogonal to the particle displacement, originating a vortex-type phenomenon.
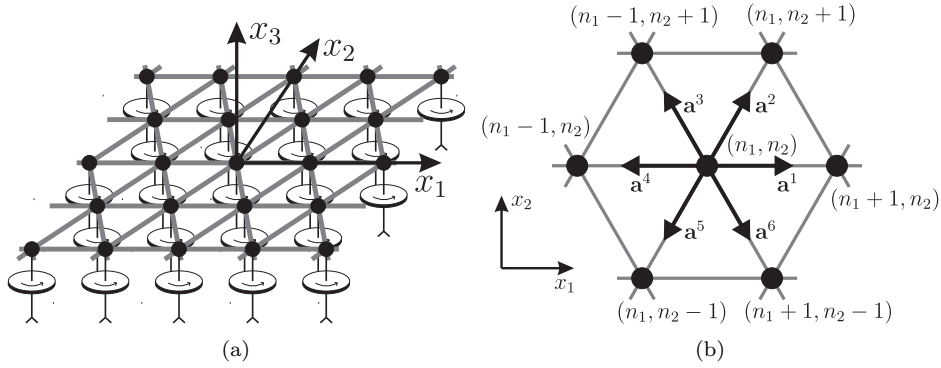

Figure 1: (a) Monatomic triangular lattice, connected to a system of gyroscopes; (b) plane representation of a lattice cell.

The periodicity of the triangular lattice is defined by the vectors

$$\mathbf{t}^1 = (l,0)^{\mathrm{T}} \ \text{ and } \ \mathbf{t}^2 = \left(l/2, \sqrt{3}\,l/2\right)^{\mathrm{T}}, \tag{1}$$

which are collected in the matrix

$$\mathbf{T} = \left(\mathbf{t}^1, \mathbf{t}^2\right) = \begin{pmatrix} l & l/2 \\ 0 & \sqrt{3}\,l/2 \end{pmatrix}. \tag{2}$$

Each particle of the lattice is identified by the multi-index $\mathbf{n} = (n_1, n_2)^{\mathrm{T}}$. Hence, its position in the plane x_1-x_2 is given by

$$\mathbf{x^n} = \mathbf{x^0} + \mathbf{Tn} = \mathbf{x^0} + n_1\mathbf{t}^1 + n_2\mathbf{t}^2. \tag{3}$$

3

As shown in Fig. 1b, the six directions of the lattice links are specified by the unit vectors

$$\mathbf{a}^1 = (1,0)^{\mathrm{T}} \;;\; \mathbf{a}^2 = \left(1/2, \sqrt{3}/2\right)^{\mathrm{T}} \;;\; \mathbf{a}^3 = \left(-1/2, \sqrt{3}/2\right)^{\mathrm{T}} \;;$$

$$\mathbf{a}^4 = (-1,0)^{\mathrm{T}} = -\mathbf{a}^1 \;;\; \mathbf{a}^5 = \left(-1/2, -\sqrt{3}/2\right)^{\mathrm{T}} = -\mathbf{a}^2 \;; \tag{4}$$

$$\mathbf{a}^6 = \left(1/2, -\sqrt{3}/2\right)^{\mathrm{T}} = -\mathbf{a}^3 .$$

In the following, it is assumed that the in-plane displacement of each particle of the lattice is time-harmonic, that is $\mathbf{U}(\mathbf{x}, t) = \mathbf{u}^{\mathbf{n}} \mathrm{e}^{\mathrm{i}\omega t}$, with ω being the radian frequency. Therefore, the equation of motion for each particle is

$$-m\,\omega^2 \mathbf{u}^{\mathbf{n}} = c \sum_{j=1}^{6} \left[\mathbf{a}^j \cdot \left(\mathbf{u}^{\mathbf{n}+\boldsymbol{\Delta}\mathbf{n}} - \mathbf{u}^{\mathbf{n}}\right)\right] \mathbf{a}^j + \mathrm{i}\,\alpha\,\omega^2 \mathbf{R}\,\mathbf{u}^{\mathbf{n}}. \tag{5}$$

Here, $\boldsymbol{\Delta}\mathbf{n}$ represents the difference between the multi-index of a generic node connected to node $\mathbf{n}$ and the multi-index $\mathbf{n}$ (refer to Fig. 1b), while $\mathbf{R}$ is the rotation matrix

$$\mathbf{R} = \begin{pmatrix} 0 & 1 \\ -1 & 0 \end{pmatrix} \tag{6}$$

describing the vorticity effect induced by the gyros. The quantity α appearing in Eq. (5) is the spinner constant. It was determined by Brun et al. (2012) under the assumption that the nutation angle of the gyro varies harmonically in time with the same frequency as the lattice ω.

Bloch-Floquet conditions require that

$$\mathbf{u}\left(\mathbf{x} + n_1 \mathbf{t}^1 + n_2 \mathbf{t}^2\right) = \mathbf{u}\left(\mathbf{x}\right) \mathrm{e}^{\mathrm{i}\,\mathbf{k}\cdot\mathbf{T}\mathbf{n}}, \tag{7}$$

where $\mathbf{k} = (k_1, k_2)^{\mathrm{T}}$ is the Bloch (or wave) vector. The introduction of Eq. (7) into Eq. (5) leads to

$$-m\,\omega^2 \mathbf{u}^{\mathbf{n}} = c \sum_{j=1}^{6} \left(\mathbf{a}^j \otimes \mathbf{a}^j\right) \mathbf{u}^{\mathbf{n}} \left(\mathrm{e}^{\mathrm{i}\,\mathbf{k}\cdot\mathbf{T}\boldsymbol{\Delta}\mathbf{n}} - 1\right) + \mathrm{i}\,\alpha\,\omega^2 \mathbf{R}\,\mathbf{u}^{\mathbf{n}}, \tag{8}$$

where the symbol $\otimes$ stands for the dyadic vector product.

Eq. (8) has a non-trivial solution provided that

$$\left(m^2 - \alpha^2\right) \omega^4 - m\,\mathrm{tr}(\mathbf{C})\,\omega^2 + \det(\mathbf{C}) = 0, \tag{9}$$

where $\mathbf{C}$ is the stiffness matrix

$$\mathbf{C} = c \begin{pmatrix} 3 - 2\cos(k_1 l) - \frac{\cos(\zeta)+\cos(\xi)}{2} & \frac{\sqrt{3}[\cos(\xi)-\cos(\zeta)]}{2} \\ \frac{\sqrt{3}[\cos(\xi)-\cos(\zeta)]}{2} & 3 - \frac{3[\cos(\zeta)+\cos(\xi)]}{2} \end{pmatrix}, \tag{10}$$

with

$$\zeta = k_1 l/2 + \sqrt{3}k_2 l/2 \quad \text{and} \quad \xi = k_1 l/2 - \sqrt{3}k_2 l/2. \tag{11}$$

Eq. (9) is the dispersion relation of the chiral medium, and it is analysed in detail in the next section.

4

3. Dispersion properties

Since c, m and α are real and positive quantities, the biquadratic equation (9) in ω admits two positive solutions (which define two dispersion surfaces) if $\alpha < m$. The lower and upper dispersion surfaces are denoted by $\omega_1(\mathbf{k})$ and $\omega_2(\mathbf{k})$, respectively. On the other hand, if $\alpha > m$ Eq. (9) yields a single real positive solution ($\omega_1(\mathbf{k})$), while the second solution ($\omega_2(\mathbf{k})$) is imaginary. The regimes $\alpha < m$ and $\alpha > m$ will henceforth be designated "subcritical" and "supercritical", respectively.

In the following, all the physical quantities will be normalised by the natural units of the system, which will be assigned unit values: $m = 1$, $c = 1$, $l = 1$. Accordingly, physical units of measurement will not be shown.

3.1. Dispersion surfaces

The explicit expressions of the dispersion surfaces obtained from Eq. (9) are the following:

$$\omega_1(\mathbf{k}) = \sqrt{\frac{\mathrm{tr}(\mathbf{C}) - \sqrt{\mathrm{tr}^2(\mathbf{C}) - 4(1 - \alpha^2)\det(\mathbf{C})}}{2(1 - \alpha^2)}}; \qquad (12\mathrm{a})$$

$$\omega_2(\mathbf{k}) = \sqrt{\frac{\mathrm{tr}(\mathbf{C}) + \sqrt{\mathrm{tr}^2(\mathbf{C}) - 4(1 - \alpha^2)\det(\mathbf{C})}}{2(1 - \alpha^2)}}. \qquad (12\mathrm{b})$$

In a non-chiral lattice, $\omega_1(\mathbf{k})$ and $\omega_2(\mathbf{k})$ are associated with pure shear and pure pressure waves, respectively. If a system of gyros is introduced, the waves are polarised, as discussed in Section 3.3.

The dispersion surfaces are plotted in Figs. 2a-2c for different values of the spinner constant α. More specifically, Figs. 2a and 2b refer to the subcritical regime ($\alpha = 0.3, 0.6$), while Fig. 2c shows a case in the supercritical regime ($\alpha = 2.0$). Figs. 2d-2f represent the cross-sections, for $k_2 = 0$, of the dispersion surfaces drawn in Figs. 2a-2c.

Fig. 2 shows that, in the subcritical regime ($\alpha < 1$), ω_2 extends to higher values as α increases, while ω_1 slightly flattens. As $\alpha \to 1$, $\omega_2 \to \infty$. In the supercritical regime ($\alpha > 1$), the dispersion surface ω_2 does not exist and only ω_1 remains (see Figs. 2c and 2f); hence, the waves are of the shear type. Finally, when $\alpha \to \infty$, ω_1 becomes flat and tends to zero for every wave vector $\mathbf{k}$.

In order to better understand the properties of ω_1 and ω_2, the phase velocities for both the dispersion surfaces are determined near the origin ($\mathbf{k} \to \mathbf{0}$), where the medium does not behave in a dispersive way. In a neighbourhood of $\mathbf{k} = \mathbf{0}$ the asymptotic expressions of the phase velocities are

$$c_1^{ph} = \sqrt{\frac{3\left(2 - \sqrt{1 + 3\,\alpha^2}\right)}{8\left(1 - \alpha^2\right)}}; \qquad (13\mathrm{a})$$

$$c_2^{ph} = \sqrt{\frac{3\left(2 + \sqrt{1 + 3\,\alpha^2}\right)}{8\left(1 - \alpha^2\right)}}. \qquad (13\mathrm{b})$$
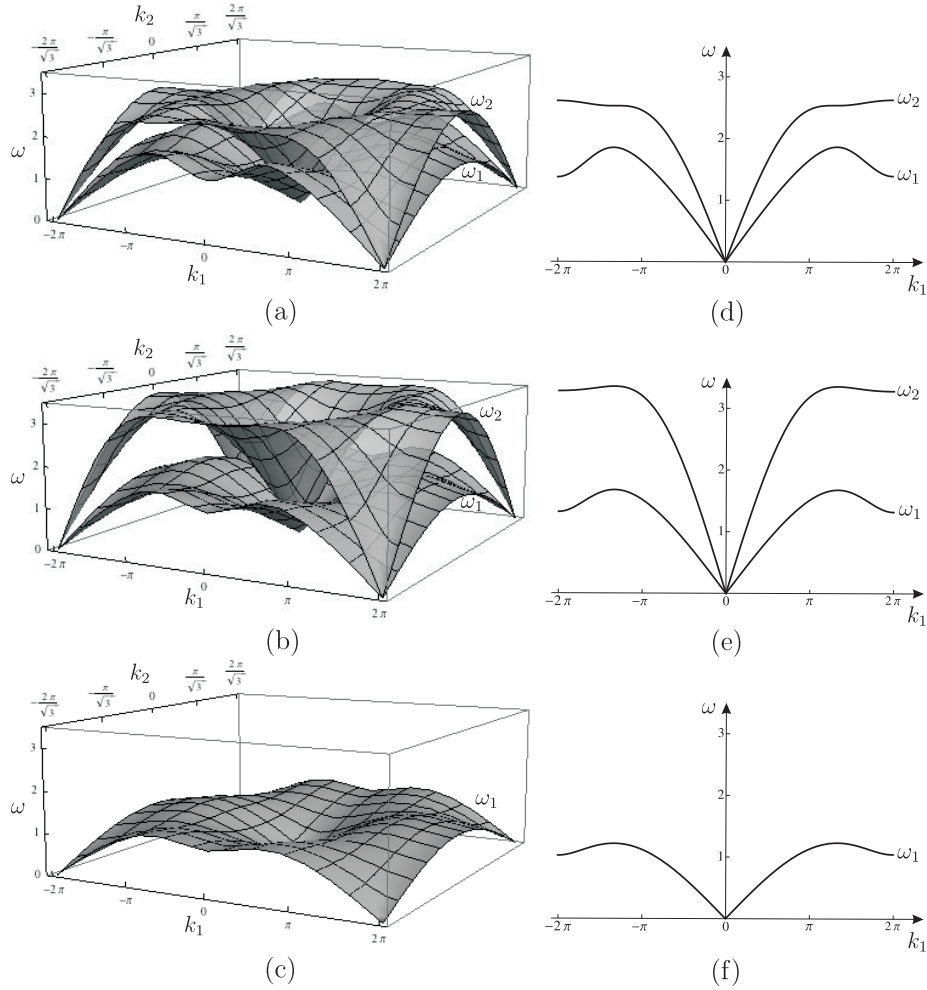
Figure 2: Dispersion surfaces (a-c) and relative cross-sections for $k_2 = 0$ (d-f) for different values of the spinner constant: $\alpha = 0.3$ (a,d); $\alpha = 0.6$ (b,e); $\alpha = 2.0$ (c,f).

The above functions of α are plotted in Fig. 3. The phase velocity associated with ω_1 (c_1^{ph}) decreases for increasing values of α, thus exhibiting a "softening" behaviour of the medium. On the other hand, c_2^{ph} is augmented by increasing α, until it tends to infinity as $\alpha \to 1$. Therefore, one of the main effects of the system of gyros is to "stiffen" the lattice with respect to the propagation of waves dominated by pressure. This feature of the chiral lattice may have important implications in practical applications, as this vortex-type medium can be used as a "pressure wave accelerator".
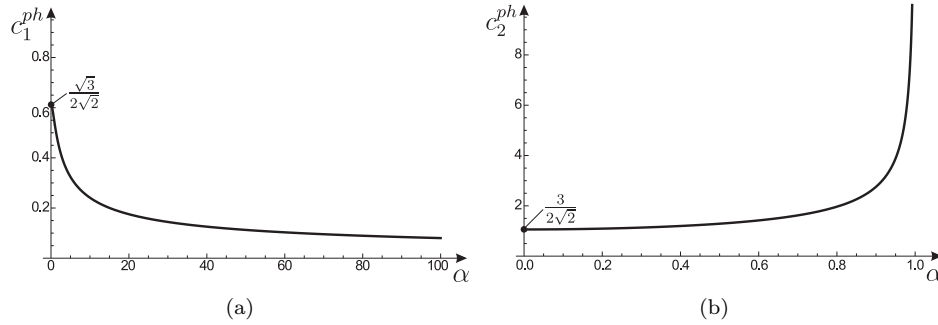
6

Figure 3: Phase velocities in the neighbourhood of the origin of the irreducible Brillouin zone as a function of the spinner constant α. Results correspond to dispersion surfaces ω_1 (a) and ω_2 (b). Note the different ranges of the variables in the two figures.

3.2. Stationary points of the dispersion surfaces

In this section, the stationary points of the dispersion surfaces are determined and classified according to their type. The values of the dispersion surfaces at the stationary points correspond to the frequencies of the standing waves of the model.

The positions of the stationary points in the reciprocal space are shown in Fig. 4. Points A-E (represented by crosses) stay fixed in the k_1-k_2 plane as the spinner constant α is varied, while points F and G (indicated by dots) change their positions at increasing α. In particular, for $\alpha < 1/3$, F is located between O and D, while G is between E and V; for $\alpha = 1/3$, F coincides with D, while G coincides with E; for $1/3 < \alpha < \sqrt{7/27}$, F is found between D and A, while G is between B and E; finally, for $\alpha \geq \sqrt{7/27}$ F and G coincide with A and B, respectively.

The stationary points of the lower dispersion surface ω_1 are the points A-E. These points can be classified into two types, as detailed in Table 1, where their coordinates in the reciprocal space are also reported. In the lower dispersion surface ω_1 each stationary point remains of the same type, saddle point or maximum, as α varies. The cross-sections of ω_1 along the path ODAV (shown in Fig. 4) are plotted in Fig. 5 for different values of α. The curves show stationary points representative of classes I and II.

For the upper dispersion surface ω_2, the type of the stationary points A-E varies with α, as specified in Table 2. Two additional stationary points F and G appear. These are saddle points having a position in the reciprocal space changing with α and detailed in Table 2. The cross-sections of ω_2 along the path ODAV are plotted in Fig. 6 for different values of α. The curves show stationary points representative of classes III, IV and V.

3.3. Polarisation

In the two-dimensional triangular lattice without gyros ($\alpha = 0$), the dispersion relation (12a) represents pure shear waves, polarised orthogonal to the wave
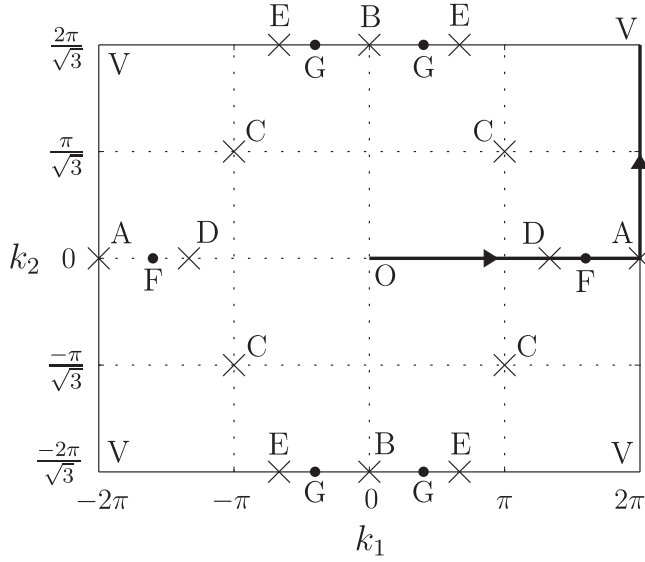
7

Figure 4: Positions of the stationary points in the k_1-k_2 plane for $\alpha = 0.45$ (the crosses indicate fixed points, while the dots represent points moving with α).

class	point	k_1	k_2	ω_1	type (for any α)
I	A	$\pm 2\pi$	0	$\sqrt{\dfrac{6}{2+\sqrt{1+3\alpha^2}}}$	saddle points
	B	0	$\pm\frac{2\pi}{\sqrt{3}}$		
	C	$\pm\pi$	$\pm\frac{\pi}{\sqrt{3}}$		
II	D	$\pm\frac{4\pi}{3}$	0	$\sqrt{\dfrac{9}{2(1+\alpha)}}$	maxima
	E	$\pm\frac{2\pi}{3}$	$\pm\frac{2\pi}{\sqrt{3}}$		

Table 1: Stationary points relative to the lower dispersion surface ω_1.

vector $\mathbf{k}$. On the other hand, dispersion relation (12b) describes pure pressure waves, because the eigenvector corresponding to the eigenvalue ω_2 is polarised parallel to the wave vector $\mathbf{k}$. The system of gyros affects the polarisation, and the dispersion relations (12) when $\alpha \neq 0$ do not represent pure shear and pure pressure waves, as discussed in the following.

The vector equation of motion (8), for $m = 1$, $c = 1$, $l = 1$, can be written explicitly as the following system of scalar equations:
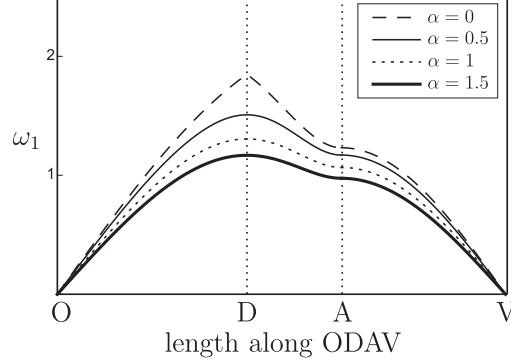
Figure 5: Sections of the lower dispersion surface ω_1 along the path ODAV, shown in Fig. 4, determined for different values of α.

class	point	k_1	k_2	ω_2	type	
					$\alpha < \sqrt{7/27}$	$\alpha > \sqrt{7/27}$
III	A	$\pm 2\pi$	0	$\sqrt{\dfrac{6}{2-\sqrt{1+3\alpha^2}}}$	maxima	saddle points
	B	0	$\pm\dfrac{2\pi}{\sqrt{3}}$			
	C	$\pm\pi$	$\pm\dfrac{\pi}{\sqrt{3}}$			
					$\alpha < 1/3$	$\alpha > 1/3$
IV	D	$\pm\dfrac{4\pi}{3}$	0	$\sqrt{\dfrac{9}{2(1-\alpha)}}$	minima	maxima
	E	$\pm\dfrac{2\pi}{3}$	$\pm\dfrac{2\pi}{\sqrt{3}}$			
					$\alpha < \sqrt{7/27}$	$\alpha > \sqrt{7/27}$
V	F	$4\arccos\left(\frac{1}{4}\sqrt{7-27\alpha^2}\right),\ \pm 2\pi$	0	$\dfrac{9}{4}\sqrt{1+3\alpha^2}$	saddle points	$\equiv$ A
	G	$4\arccos\left(\frac{3}{4}\sqrt{1+3\alpha^2}\right),\ 0$	$\pm\dfrac{2\pi}{\sqrt{3}}$			$\equiv$ B

Table 2: Stationary points of the upper dispersion surface ω_2.

$$\left[\omega^2 - 3 + 2\cos(k_1) + \frac{\cos\left(\zeta\right) + \cos\left(\xi\right)}{2}\right] u_1 + \left[\sqrt{3}\frac{\cos\left(\zeta\right) - \cos\left(\xi\right)}{2} + \mathrm{i}\,\alpha\,\omega^2\right] u_2 = 0; \quad (14\mathrm{a})$$

$$\left[\sqrt{3}\frac{\cos\left(\zeta\right) - \cos\left(\xi\right)}{2} - \mathrm{i}\,\alpha\,\omega^2\right] u_1 + \left[\omega^2 - 3 + 3\frac{\cos\left(\zeta\right) + \cos\left(\xi\right)}{2}\right] u_2 = 0. \quad (14\mathrm{b})$$

The quantities ζ and ξ in the system above have been defined in Eq. (11).

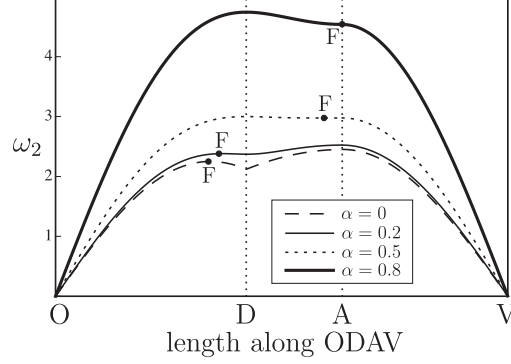In the low frequency limit, and hence for small values of $\mathbf{k}$, Eqs. (14) reduce

9

Figure 6: Sections of the upper dispersion surface ω_2 along the path ODAV, shown in Fig. 4, obtained for different values of α.

to

$$\left[\omega^2 - \frac{9}{8}k_1^2 - \frac{3}{8}k_2^2\right]u_1 - \left[\frac{3}{4}k_1k_2 - \mathrm{i}\,\alpha\,\omega^2\right]u_2 = 0; \tag{15a}$$

$$-\left[\frac{3}{4}k_1k_2 + \mathrm{i}\,\alpha\,\omega^2\right]u_1 + \left[\omega^2 - \frac{3}{8}k_1^2 - \frac{9}{8}k_2^2\right]u_2 = 0. \tag{15b}$$

The eigenvector $\mathbf{u}$, corresponding to either ω_1 or ω_2, can be expressed as $(1, \Psi)^{\mathrm{T}}$, where $\Psi = u_2/u_1$.

In order to define quantitatively the polarisation induced by the gyros, the angles γ_1 and γ_2 are introduced. As shown in Fig. 7a, γ_1 is the angle between the eigenvector $\mathbf{u}$ relative to ω_1 for $\alpha \neq 0$ and the normal to the wave vector $\mathbf{k}$ (which coincides with the direction of the eigenvector $\mathbf{u}(\omega_1)$ when $\alpha = 0$). On the other hand, γ_2 represents the angle between the eigenvector $\mathbf{u}(\omega_2)$ for $\alpha \neq 0$ and the wave vector $\mathbf{k}$ (that is parallel to $\mathbf{u}(\omega_2)$ when $\alpha = 0$), as shown in Fig. 7c. If $\mathbf{k} = (\cos(\beta), \sin(\beta))^{\mathrm{T}}$, where β can vary between 0 and 2π,

$$\gamma_1 = \frac{\pi}{2} - \arccos\left|\frac{k_1 + \Psi(\omega_1)k_2}{\sqrt{1 + \Psi(\omega_1)\bar{\Psi}(\omega_1)}}\right|, \tag{16a}$$

$$\gamma_2 = \arccos\left|\frac{k_1 + \Psi(\omega_2)k_2}{\sqrt{1 + \Psi(\omega_2)\bar{\Psi}(\omega_2)}}\right|, \tag{16b}$$

where $\bar{\Psi}$ is the complex conjugate of Ψ.

In the low frequency limit, both γ_1 and γ_2 do not change with the orientation of the wave vector, defined by β. This is due to the fact that, near the origin of the reciprocal space, the chiral lattice behaves as an isotropic medium. The variations of γ_1 and γ_2 with the spinner constant α are shown in Figs. 7b and 7d, respectively. It can be seen that, if $\alpha = 0$ (i.e. if the gyros are removed from the lattice), γ_1 and γ_2 are both zero, therefore the waves travelling in the medium are of pure shear and pressure types. When the gyros are attached to the lattice particles, the waves are polarised, since γ_1 and γ_2 become non zero. The angles
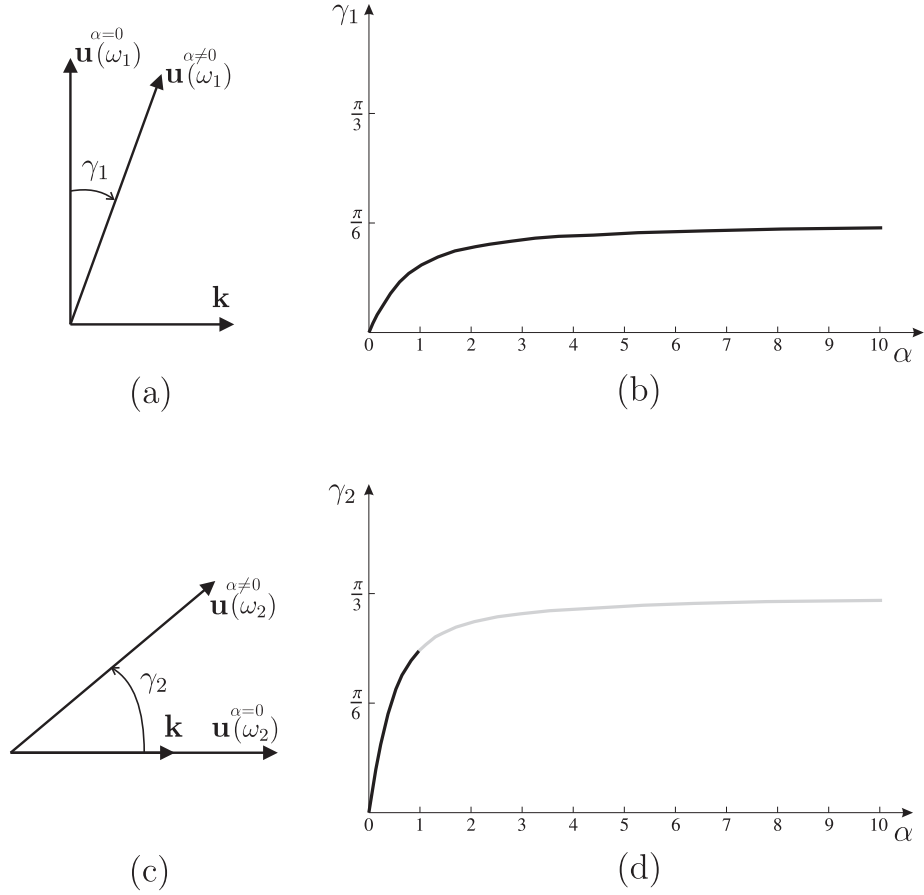
10

Figure 7: (a) Definition of the angle γ_1; (b) dependence of γ_1 on the spinner constant α; (c) definition of the angle γ_2; (d) dependence of γ_2 on α, where the grey part of the diagram indicates that waves are evanescent in the supercritical regime $\alpha > 1$.

γ_1 and γ_2 increase monotonically with α. In the limit for $\alpha \to \infty$, $\gamma_1 \to \pi/6$, while $\gamma_2 \to \pi/3$, so that waves with frequencies ω_1 and ω_2 are aligned in this limit and polarised with an angle of $\pi/3$ with respect to the direction of wave propagation. Actually, we point out that the dispersion surface ω_2 corresponds to propagating waves only in the subcritical regime $\alpha < 1$, and $\gamma_2 = \pi/4$ at the critical regime $\alpha = 1$. Finally, we observe that, for any given value of α, γ_2 is larger than γ_1. Thus, the gyros act as "shear polarisers".

For large values of $\mathbf{k}$, the eigenvector must be calculated by using Eqs. (14) instead of Eqs. (15). At higher frequencies, the medium exhibits a dynamic anisotropic behaviour. To clarify this point, the slowness contours $\omega_1(\mathbf{k}) = 1$, calculated for $\alpha = 0.9$ (solid line) and $\alpha = 0$ (dashed line), are plotted in Fig. 8a. The angle γ_1 varies with the angle β (which identifies the direction of wave propagation), as can be seen from Fig. 8b (here only the range $\pi/6 \leq \beta \leq \pi/2$

11

has been considered on the horizontal axis due to the symmetry of the slowness contours). This anisotropy is observed for both cases $\alpha = 0.9$ (solid line) and $\alpha = 0$ (dashed line). However, for any α, the average value of γ_1 is close to the value shown in Fig. 7b, where it was obtained for $\mathbf{k} \to \mathbf{0}$. Similar considerations can be applied to the dispersion surface $\omega_2(\mathbf{k})$.
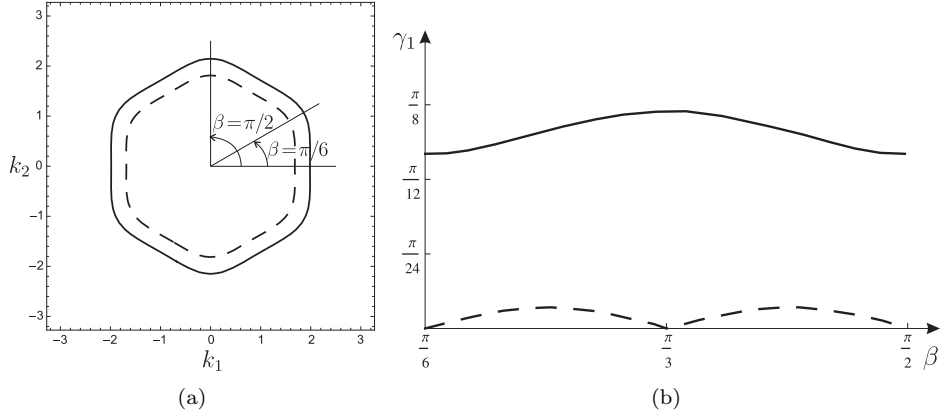

(a)   (b)

Figure 8: (a) Slowness contours $\omega_1(\mathbf{k}) = 1$, obtained for $\alpha = 0.9$ (solid line) and $\alpha = 0$ (dashed line); (b) relations between polarisation angle γ_1 and wave vector angle β for $\alpha = 0.9$ (solid line) and $\alpha = 0$ (dashed line), evaluated in the sector $\pi/6 \leq \beta \leq \pi/2$.

3.4. Standing waves at the saddle points

Saddle points of the dispersion surfaces are associated with very strong dynamic anisotropy. In fact, waves with a frequency close to the frequency of the saddle points propagate along the preferential directions defined by the geometry of the medium. In order to visualise the preferential directions of the triangular lattice of Fig. 1, the eigenmodes corresponding to the saddle points frequencies of both ω_1 and ω_2 are shown. They can be obtained from either of Eqs. (14).

Firstly, the lower dispersion surface $\omega_1(\mathbf{k})$ is considered. The slowness contour for $\alpha = 0.9$, determined at the frequency of the saddle points A-C (belonging to class I of Table 1), is plotted in Fig. 9a, where the saddle points are indicated by dots. The undeformed and deformed cells at the saddle points A, C1 and C2 are shown in Figs. 9b-9d, respectively.

The three preferential directions of the triangular lattice are clearly visible from Figs. 9b-9d, which also show that the waves are dominated by shear. The same preferential directions are found in a non-chiral lattice ($\alpha = 0$), although at a different value of the frequency ($\omega = \sqrt{2}$). Nonetheless, the introduction of the gyros generates an additional rotation of the points around their initial positions, so that the total deformation is not of pure shear type. This effect of the gyros can be seen from Figs. 9c and 9d, and it is better shown in the videos included in the electronic supplementary material accompanying this paper (see videos1.zip).
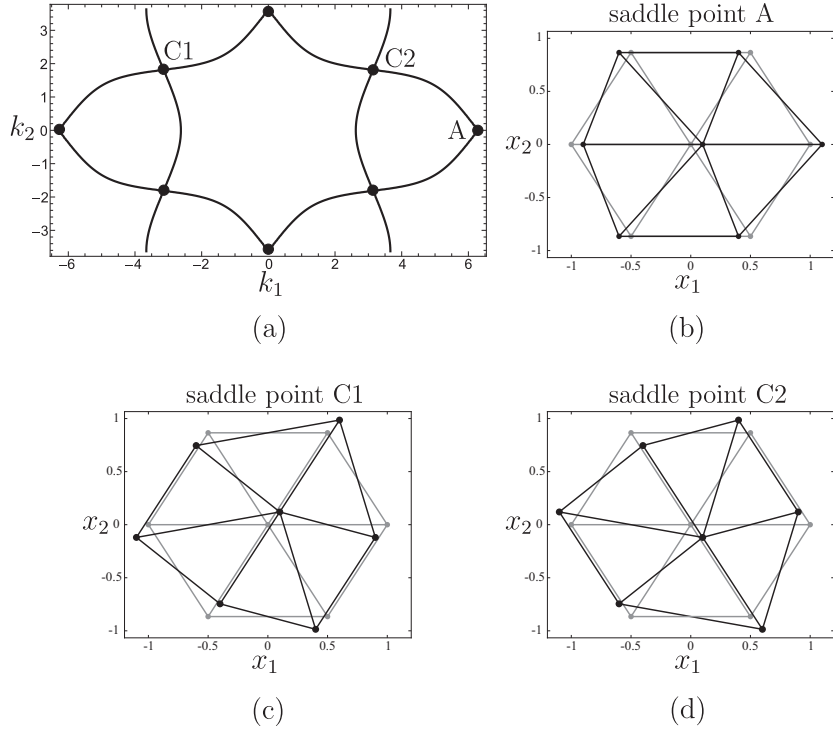
12

(a)

(b)

(c)

(d)

Figure 9: (a) Slowness contour $\omega_1 = \sqrt{6/(2 + \sqrt{1 + 3\,\alpha^2})}$ for $\alpha = 0.9$; the heavy dots represent the saddle points. (b)-(d) Standing modes at the saddle points A, C1 and C2, specified in (a). The modes (in black) are shown together with the undeformed lattice (in grey).

For the upper dispersion surface $\omega_2(\mathbf{k})$, the slowness contour for $\alpha = 0.9$, obtained at the frequency of the stationary points A-C (class III of Table 2), is drawn in Fig. 10a. The standing waves at the saddle points A, C1 and C2 are represented in Figs. 10b-10d. Also in this case, there are three preferential directions, but the waves are of the pressure type. As in the case of ω_1, the gyros make the lattice particles rotate around their positions, as can be better seen in the supplementary material (see videos2.zip).

3.5. Critical regime: asymptotic analysis for $\alpha \simeq m$

The degenerate case $\alpha \simeq m$ is of particular interest. Let ϵ define a small quantity $(0 < \epsilon \ll 1)$ such that $\alpha = 1 \pm \epsilon$ $(m = 1)$. If $\alpha = 1 - \epsilon$ (subcritical regime), there are two dispersion surfaces, which have the following asymptotic
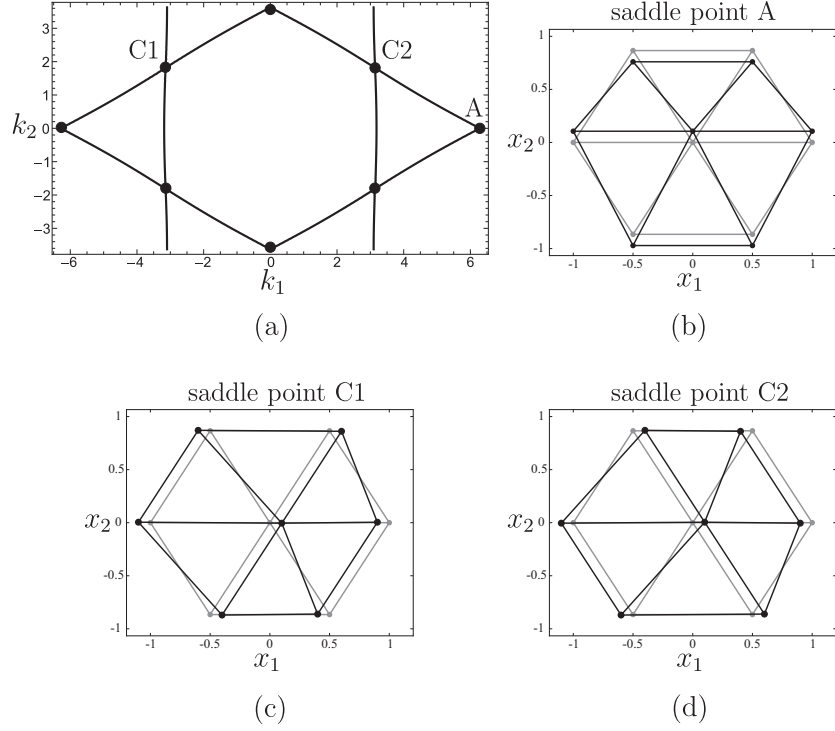
13

Figure 10: (a) Slowness contour $\omega_2 = \sqrt{6/(2 - \sqrt{1 + 3\,\alpha^2})}$ for $\alpha = 0.9$; the saddle points at this frequency are indicated by heavy dots. (b)-(d) Standing modes at the saddle points A, C1 and C2, specified in (a). The modes (in black) are shown together with the undeformed lattice (in grey).

representations:

$$\omega_1 \simeq \sqrt{\frac{\det(\mathbf{C})}{\operatorname{tr}(\mathbf{C})}} =$$

$$= \frac{\sqrt{3}}{2} \sqrt{\frac{6 - 3\cos(k_1) - 2\left[3\cos\left(\frac{k_1}{2}\right) - \cos\left(\frac{3k_1}{2}\right)\right]\cos\left(\frac{\sqrt{3}k_2}{2}\right) + \cos\left(\sqrt{3}k_2\right)}{3 - \cos(k_1) - 2\cos\left(\frac{k_1}{2}\right)\cos\left(\frac{\sqrt{3}k_2}{2}\right)}}; \qquad (17a)$$

$$\omega_2 \simeq \sqrt{\frac{\operatorname{tr}(\mathbf{C})}{2}} \frac{1}{\sqrt{\epsilon}} = \sqrt{3 - \cos(k_1) - 2\cos\left(\frac{k_1}{2}\right)\cos\left(\frac{\sqrt{3}k_2}{2}\right)} \frac{1}{\sqrt{\epsilon}}. \qquad (17b)$$

The lower dispersion surface ω_1 is independent of ϵ. On the other hand, the upper dispersion surface $\omega_2 \to \infty$ as $1/\sqrt{\epsilon}$. It must also be noted that the coefficient $\sqrt{\operatorname{tr}(\mathbf{C})/2} = 0$ at $\mathbf{k} = (\pm 2\pi, \pm 2\pi/\sqrt{3})^{\mathrm{T}}$.

If $\alpha = 1 + \epsilon$ (supercritical regime), ω_1 is still expressed by Eq. (17a), while ω_2 assumes imaginary values:

$$\omega_2 = \mathrm{i}\sqrt{\frac{\operatorname{tr}(\mathbf{C})}{2}} \frac{1}{\sqrt{\epsilon}}. \qquad (18)$$

In this regime, waves associated to ω_2 are evanescent, thus it is of interest to determine the coefficient of attenuation. There is a solution of Eq. (18) where the frequency ω_2 is real and the wave vector $\mathbf{k} = i\,r\,(\cos(\beta),\sin(\beta))^\mathrm{T}$ is purely imaginary, with β being the orientation of $\mathbf{k}$ relative to the coordinate axis x_1 and r the coefficient of attenuation. This real frequency ω_2 is found from the following equation:

$$\omega_2^2 + \frac{1}{\epsilon}\left\{3 - \cosh\left[r\cos(\beta)\right] - 2\cosh\left[\frac{r\cos(\beta)}{2}\right]\cosh\left[\frac{\sqrt{3}\,r\sin(\beta)}{2}\right]\right\} = 0, \qquad (19)$$

which also gives the representation of r as a function of ω_2, ϵ and β. The dependence of the attenuation coefficient r on the orientation of the wave vector β is due to the dynamic anisotropy of the lattice.

The relation between r and ω_2 is shown in Fig. 11 for $\epsilon = 0.1$ and two different values of β. As β varies in the interval $[0, 2\pi)$, $|r|$ varies within the lower limit

$$|r_{\min}| = 2\left|\mathrm{arccosh}\left(\frac{\sqrt{9 + 2\,\epsilon\,\omega_2^2} - 1}{2}\right)\right| \qquad (20)$$

at $\beta = 0 + n\,\pi/3$ (n integer) and the upper limit

$$|r_{\max}| = \frac{2}{\sqrt{3}}\left|\mathrm{arccosh}\left(\frac{2 + \epsilon\,\omega_2^2}{2}\right)\right| \qquad (21)$$

at $\beta = \pi/6 + n\,\pi/3$ (n integer). Note that the absolute values of r have been reported, since the sign of r depends on the angle between the position vector $\mathbf{x}$ and the direction of the wave propagation defined by $\mathbf{k}$; in particular, the sign of r must satisfy proper radiation conditions. The limiting expressions $|r_{\min}|$ and $|r_{\max}|$ as a function of the frequency ω_2 are shown in Fig. 11, where the usual inverse exponential dependence of the attenuation factor on the frequency is shown.
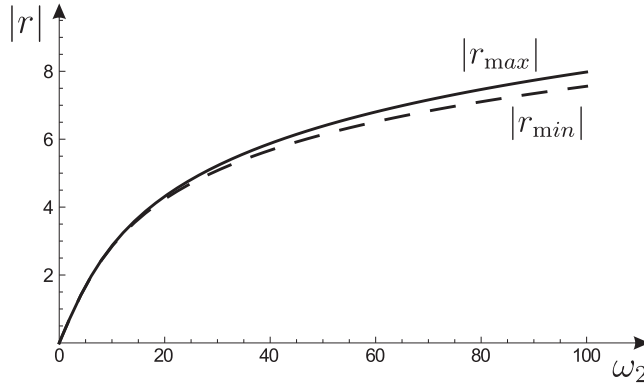

Figure 11: Attenuation coefficient $|r|$ versus frequency ω_2 for $\beta = 0 + n\,\pi/3$ ($|r_{\min}|$) and $\beta = \pi/6 + n\,\pi/3$ ($|r_{\max}|$). The curves are given for $\epsilon = 0.1$.

15

4. Simulations of frequency response problems for a chiral discrete system

In this section, the response of an infinite chiral lattice under an external harmonic excitation is analysed numerically. A finite element code has been implemented in COMSOL Multiphysics, where the gyroscopic term in the equation of motion (i.e. the last term in Eq. (5)) is introduced in the model as an equivalent external force applied to each node of the lattice with magnitude proportional to the displacement magnitude.

In order to simulate an infinite lattice, a computational domain consisting of 60 triangular elements in the horizontal direction and 68 elements in the vertical direction has been modelled. To avoid reflections from the boundaries, the lattice links of the five layers of elements closest to the boundaries are connected to viscous dampers. In this way, waves are absorbed before impinging on the boundaries and the viscous dampers play the role of "perfectly matched layers", as in Carta et al. (2013). We note that the viscosity coefficient of the dampers has been tuned in order to minimise reflections.

The lattice is excited by a vertical or horizontal harmonic displacement of unit amplitude applied at the central node of the model.

Low frequency regime. Firstly, a low excitation frequency is considered. In the low frequency range, the lattice behaves as an isotropic medium. Fig. 12 shows the displacement amplitude fields determined for different values of the spinner constant α, with $\omega = 0.5$. In particular, Figs. 12a and 12b refer to the subcritical regime ($\alpha = 0$ and $\alpha = 0.5$, respectively), Fig. 12c considers the critical case ($\alpha = 1$), while Fig. 12d presents an example in the supercritical regime ($\alpha = 1.5$).

Fig. 12a represents the typical low-frequency wave pattern produced by a point source in a non-chiral medium ($\alpha = 0$). In the direction of the excitation, waves are characterised by a larger wavelength, thus they are of the pressure type. In the perpendicular direction waves present a shorter wavelength, hence they are dominated by shear. In the presence of gyros, a vortex appears around the point source; the directional preference of shear and pressure waves is less evident, with shear waves being dominant, as can be seen from Fig. 12b ($\alpha = 0.5$). In the critical case $\alpha = 1$, the wave pattern is nearly isotropic, as shown by Fig. 12c. Finally, in the supercritical case $\alpha = 1.5$, waves are of the shear type, being characterised by a small wavelength, as demonstrated by Fig. 12d.

The vortex-type phenomenon induced by the gyros can be observed more clearly from the video files provided as the supplementary material with this manuscript (see videos3.zip). Similar wave patterns have been observed for a continuous chiral medium (see Fig. 8 of Brun et al., 2012).

Effect of the spinner parameter α on stationary points. Change in α influences substantially the dispersion properties of the Bloch waves in the chiral lattice. Here we give several indicative examples, which include the critical points on the dispersion surface (i.e. those corresponding to standing waves) of both types: the points of maximum and the saddle points, both associated with the same Bloch vector in the reciprocal lattice. In particular, we consider
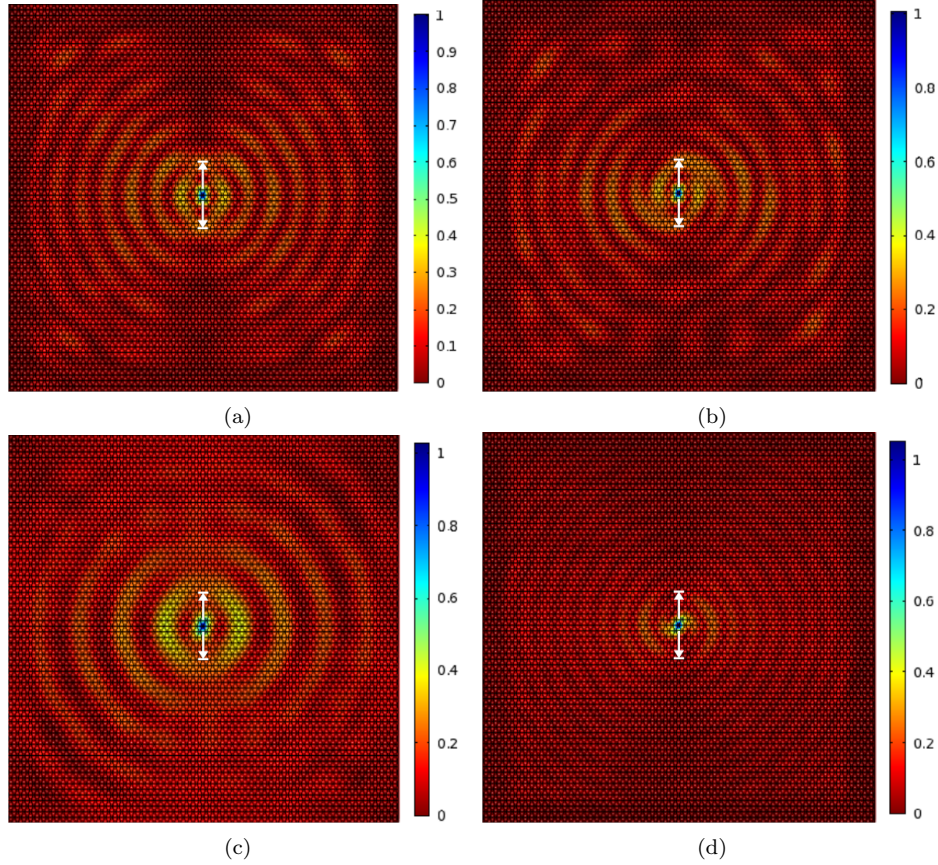
Figure 12: Displacement magnitude fields produced by a vertical harmonic displacement of low frequency $\omega = 0.5$, imposed on the central node of the lattice. The displacement fields are given for different values of the spinner constant: (a) $\alpha = 0$; (b) $\alpha = 0.5$; (c) $\alpha = 1$; (d) $\alpha = 1.5$. (Online version in colour.)

stationary points of class III in Table 2.

In Figs. 13a and 13b, two regimes for $\alpha = 0$ and a subcritical positive α are presented. The corresponding point on the dispersion diagram is a point of maximum. However, when a forced vibration is initiated at the given frequency, the chiral case is characterised by a larger region of influence and weaker localisation compared to the case of the non-chiral medium (when $\alpha = 0$).

Figs. 13c and 13d correspond to a saddle point. The spinner constant α is equal to 0.9 and the lattice is excited by a vertical or a horizontal unit displacement vibrating harmonically. The lattice exhibits a dynamically anisotropic behaviour, which has been tuned by increasing the spinner constant α, so that the type of stationary point changed from a maximum to a saddle point. In this case waves tend to propagate along preferential directions defined by the lattice geometry, whereas propagation along the other directions is suppressed.
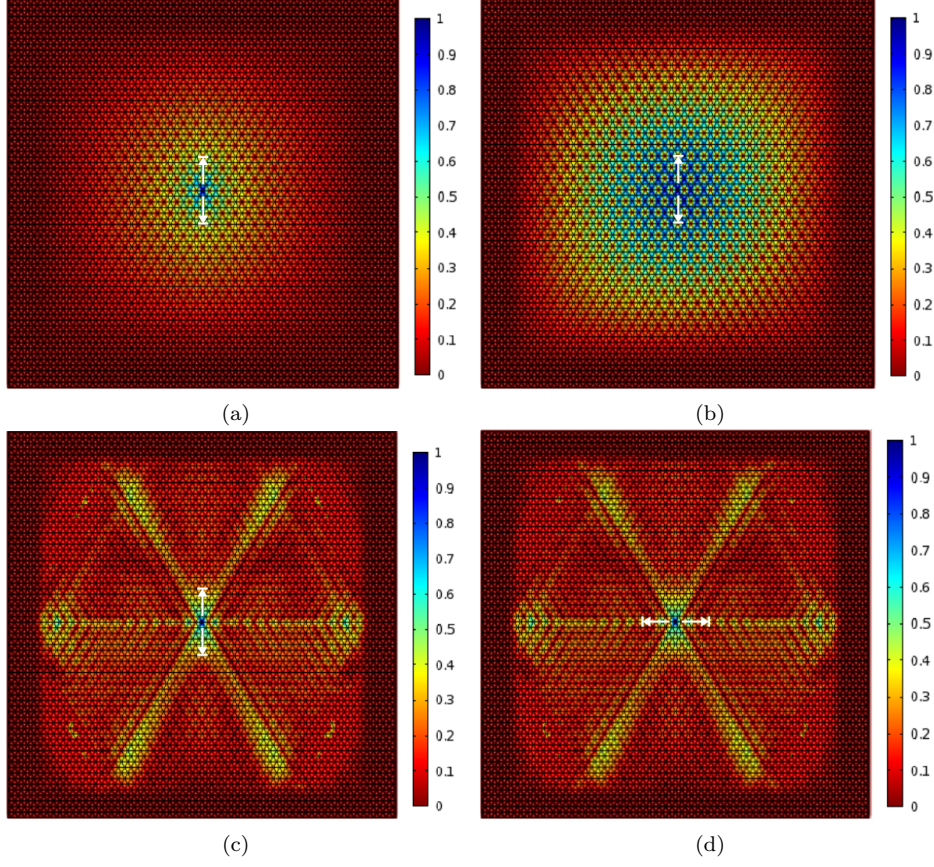
Figure 13: Displacement amplitudes as a result of an applied unit displacement varying harmonically at the stationary points frequency $\omega = \sqrt{6/(2 - \sqrt{1 + 3\alpha^2})}$ (see Table 2, class III). The subcritical spinner constant is: (a) $\alpha = 0$; (b) $\alpha = 0.2$; (c-d) $\alpha = 0.9$. (a), (b) and (c) correspond to an applied vertical displacement and (d) to an applied horizontal one. (Online version in colour.)

In both cases, the three preferential directions of propagation are clearly identified. They coincide with those obtained analytically in Section 3.4 (see Fig. 10). Similar numerical results have been found by Colquitt et al. (2012) in a non-chiral triangular lattice, in which the links are Euler-Bernoulli beams (see Fig. 8 in the cited paper). Hovewer, in Colquitt et al. (2012) the non-chiral medium responds differently to different excitations, while here the differences between the diagrams in Figs. 13c and 13d are negligibly small. Hence, the direction of the applied force does not influence the vibration pattern of the star-shaped wave form.

Critical regime for α in the transition region. With reference to Table 2, we give illustrations for the cases when α is chosen in the neighbourhood of $\sqrt{7/27}$. The case $\alpha = \sqrt{7/27}$ is important for the upper dispersion surface

18

dominated by pressure waves; namely, the saddle points F and G shown in Fig. 4 coincide with A and B, respectively, in the limit when $\alpha \to \sqrt{7/27}$. Moreover, the points A, B and C become the saddle points on the upper dispersion surface as $\alpha > \sqrt{7/27}$, and hence the dynamic anisotropy may be observed in the neighbourhood of $\omega = \sqrt{6/(2 - \sqrt{1 + 3\alpha^2})}$.

The next computations correspond to a small perturbation of the spinner constant, which results in a dramatic change of the dynamic response of the elastic system. The vibrations are initiated by a vertical unit displacement applied at the central nodal mass, at the frequency $\omega = \sqrt{6/(2 - \sqrt{1 + 3\alpha^2})}$. Fig. 14a corresponds to a point of maximum (for $\alpha < \sqrt{7/27}$); the displacement field does not represent a propagating wave, instead a localisation is observed. Fig. 14b shows the case of the saddle point (for $\alpha > \sqrt{7/27}$), and hence preferential directions of the wave propagation are clearly identified. Again, the three preferential directions visible on Fig. 14b are similar to the computations in Colquitt et al. (2012), and these preferential directions are governed by the slowness contour shown in Fig. 10a.

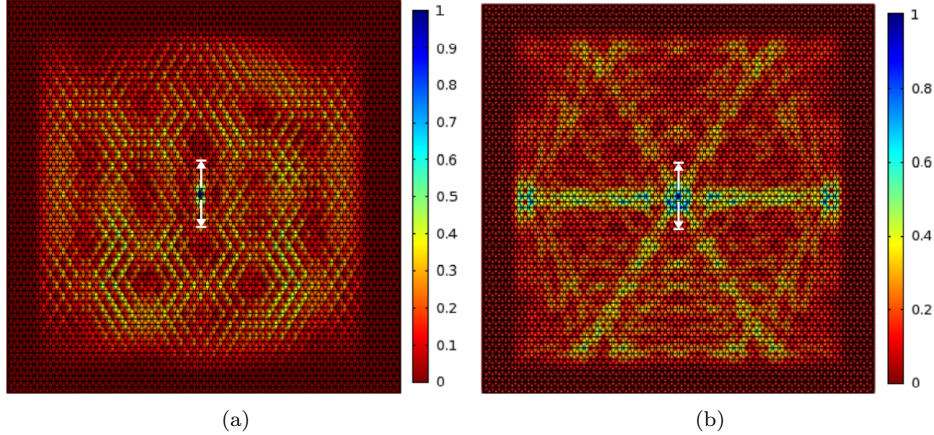(a)   (b)

Figure 14: Displacement amplitudes as a result of an applied vertical unit displacement vibrating harmonically at the stationary points frequency $\omega = \sqrt{6/(2 - \sqrt{1 + 3\alpha^2})}$. The subcritical spinner constants are close to the transition value $\alpha = \sqrt{7/27}$: (a) $\alpha = \sqrt{7/27} - 1/10$; (b) $\alpha = \sqrt{7/27} + 1/10$. (Online version in colour.)

Response influenced by change of α for a fixed frequency. Finally, we set a frequency response simulation for a fixed frequency, while the spinner constant changes its values. The normalised radian frequency is chosen to be $\omega = 1.27$, and it is represented by the dashed horizontal line in Fig. 15a together with the dispersion curves ω_1 and ω_2 represented for different values of α. While $\alpha = 0$, i.e. the lattice is non-chiral, the normalised time-harmonic vertical displacement applied to the central nodal mass generates the response shown in Fig. 15b; the directional preference of shear and pressure waves as in Fig.
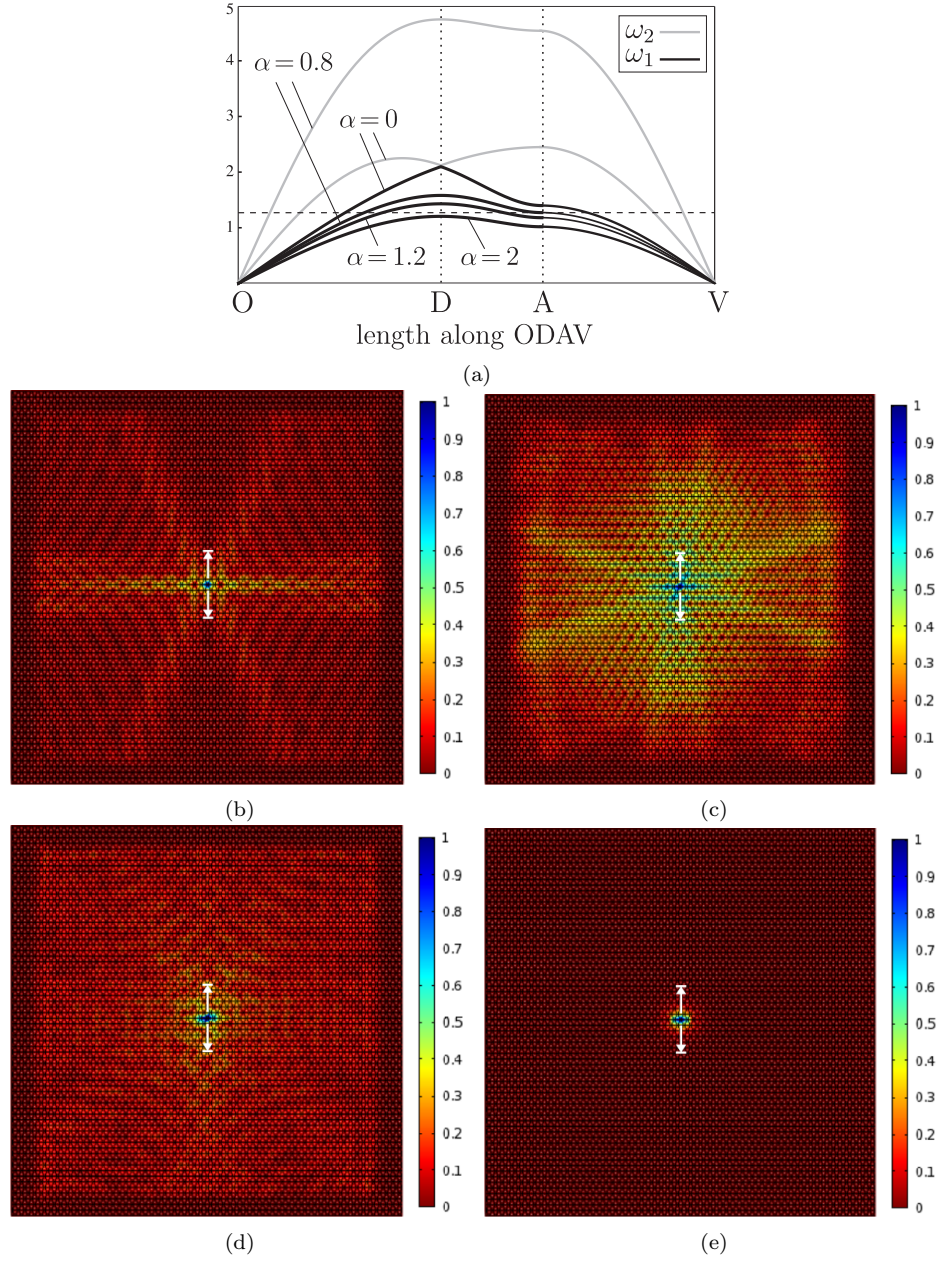
Figure 15: (a) Dispersion curves ω_1 (in black) and ω_2 (in grey) along the path ODAV indicated in Fig. 4. The curves are given for spinner constant $\alpha = 0$, 0.8, 1.2, 2.0 corresponding to part (b-e) of the figure, respectively. (b-e) Displacement amplitudes in the chiral lattice as a result of an applied vertical unit displacement at frequency $\omega = 1.27$, represented in part (a) with a dashed line. (Online version in colour.)

12a is expected, and the horizontal axis incorporates relatively large values of shear stress. In addition, three preferential directions appear; this is due to the fact that the frequency is close to the frequency of the saddle point in A for ω_1, and in the neighbourhood of A the group velocity magnitude is small. With the increase of the spinner constant to the value $\alpha = 0.8$ we achieve the configuration corresponding to a saddle point on the lower dispersion surface, as shown in Fig. 15a. The displacement magnitude is shown in Fig. 15c, and clearly indicates three preferential directions, consistent with the slowness contour in Fig. 9a. This represents the strong dynamic anisotropy discussed above. We note that the influence of the rotational action is visible in the form of a blurred central region, where anisotropy is partially suppressed due to the coupling between pressure and shear waves induced by the gyros. Further increase in α leads to Fig. 15d, where the region of influence of vibrational source is substantially reduced. We note that this case corresponds to $\alpha > 1$, and hence strong polarisation to shear waves is observed in the simulation. Fig. 15e corresponds to a sufficiently large α, such that a strong exponential localisation around the vibrational source is observed. Further increase in α will make the localisation stronger, since the given frequency value is placed in the stop band of the elastic system.

5. Conclusions

This work has demonstrated the effects of a system of gyroscopes on the dynamic properties of a monatomic lattice. The analytical findings concerning the dispersive properties of the medium have been confirmed by the illustrative results of some numerical simulations.

In a lattice containing gyros, denoted as "chiral", the formation of vortices is observed. In addition, waves are polarised, meaning that they cannot be considered as being of pure pressure or pure shear, as in a non-chiral lattice. In particular, the study of standing waves has revealed that the lattice particles do not translate, as in a non-chiral medium, but rotate around their equilibrium positions.

At high frequencies, a monatomic lattice (with or without gyros) is dynamically anisotropic, since waves tend to propagate along the preferential directions defined by the lattice geometry. These directions have been determined for both the chiral and the non-chiral lattice from the eigenmodes calculated at the saddle points of the dispersion surfaces of the medium, and have also been retrieved from the numerical computations. The value of the frequency at the stationary points depends on the spinner constant. Accordingly, the propagation band of the medium varies with the value of the spinner constant.

At low frequencies, the introduction of the gyros increases the velocity of the waves dominated by pressure and slows down the waves dominated by shear. The latter are the only waves that can propagate in the medium if the spinner constant is larger than the mass of the lattice particles.

Considering all the interesting properties described above, discrete systems with gyros can be used in engineering applications to design special dynamic

21

systems, such as wave polarisers, accelerators and decelerators of waves, and devices to guide waves along specific directions.

Acknowledgements

References

Brillouin, L., 1953. Wave propagation in periodic structures. Electric filters and crystal lattices, second ed. Dover, New York.

Brun, M., Guenneau, S., Movchan A.B., Bigoni, D., 2010. Dynamics of structural interfaces: filtering and focussing effects for elastic waves. J. Mech. Phys. Solids 58, 1212-1224.

Brun, M., Jones, I.S., Movchan, A.B., 2012. Vortex-type elastic structured media and dynamic shielding. Proc. R. Soc. A 468, 3027-3046.

Carta, G., Jones, I.S., Brun, M., Movchan, N.V., Movchan, A.B., 2013. Crack propagation induced by thermal shocks in structured media. Int. J. Solids Struct. 50, 2725-2736.

Chern, R.-L., 2013. Wave propagation in chiral media: composite Fresnel equations. J. Opt. 15, 075702 (7 pp).

Colquitt, D.J., Jones, I.S., Movchan, N.V., Movchan, A.B., 2011. Dispersion and localisation of elastic waves in materials with micro-structure. Proc. R. Soc. A 467, 2874-2895.

Colquitt, D.J., Jones, I.S., Movchan, N.V., Movchan, A.B., McPhedran, R.C., 2012. Dynamic anisotropy and localization in elastic lattice systems. Waves Random Complex Media 22, 143-159.

Thompson, W. (Lord Kelvin), 1894. The molecular tactics of a crystal. Clarendon Press, Oxford.

Kittel, C., 1956. Introduction to Solid State Physics, second ed. John Wiley & Sons, New York.

Marder, M., Liu, X., 1993. Instability in lattice fracture. Phys. Rev. Lett. 71, 2417-2420.

Martinsson, P.G., Movchan, A.B., 2003. Vibrations of lattice structures and phononic band gaps. Quart. J. Mech. Appl. Math. 56, 45-64.

Movchan, A.B., Slepyan, L.I., 2013. Resonant waves in elastic structured media: dynamic homogenisation versus Green's functions. arXiv:1310.7089.

Pendry, J.B., 2004. A chiral route to negative refraction. Science 306, 1353-1355.

Prall, D., Lakes, R.S., 1997. Properties of a chiral honeycomb with a Poisson's ratio of - 1. Int. J. Mech. Sci. 39, 305-314.

Slepyan, L.I., 2002. Models and phenomena in Fracture Mechanics. Springer, Berlin.

Spadoni, A., Ruzzene, M., Gonella, S., Scarpa, F., 2009. Phononic properties of hexagonal chiral lattices. Wave Motion 46, 435-450.